# High spatial resolution magnetic mapping using ultra-high sensitivity scanning SQUID microscopy on a speleothem from the Kingdom of Tonga, southern Pacific

**Naoto Fukuyo** ( fukuyo@aori.u-tokyo.ac.jp )
Atmosphere and Ocean Research Institute, The University of Tokyo https://orcid.org/0000-0003-2718-2943

**Hirokuni Oda**
Institute of Geology and Geoinformation, Geological Survey of Japan

**Yusuke Yokoyama**
Atmosphere and Ocean Research Institute, The Univercity of Tokyo

**Geoffrey Clark**
Archaeology and Natural History, College of Asia and the Pacific, The Australian National University

**Yuhji Yamamoto**
Center for Advanced Marine Core Research, Kochi University

**Express Letter**

**Keywords:** Scanning SQUID microscopy, paleomagnetism, environmental magnetism, speleothem, magnetite, maghemite, goethite

**Posted Date:** May 5th, 2020

**DOI:** https://doi.org/10.21203/rs.3.rs-26292/v1



**Version of Record:** A version of this preprint was published on March 23rd, 2021. See the published version at https://doi.org/10.1186/s40623-021-01401-8.

# Abstract

Speleothems can be an ideal archive of paleomagnetism because they retain continuous geomagnetic records in stable conditions and can be used for reliable radiometric dating using U-series and radiocarbon methods. However, their weak magnetic signals hinder the widespread use of this archive in the field of geoscience. While previous studies successfully reconstructed paleomagnetic signatures, including geomagnetic excursions, their time resolutions presented were still not reached to a sufficient level. Recently emerging scanning SQUID microscopy (SSM) in this field can image very weak magnetic fields while maintaining high spatial resolution that could likely overcome this obstacle. In this study, we employed SSM to conduct paleomagnetic measurements on a stalagmite collected at Anahulu cave in Tongatapu Island, the Kingdom of Tonga. The sliced sample to a thickness of ca. 0.2 mm was scan for NRM using SSM showed the influence of viscous remanent magnetization. The average measured magnetic field after 5 mT AF demagnetization is ca. 0.27 nT with a sensor-to-sample distance of ~200 μm. A stronger magnetic field (average: ca. 0.62 nT) was observed above the grayish surface layer, as compared to that of the white inner layer (average: ca. 0.09 nT) associated with the laminated structures of a speleothem at the submillimeter scale with the SSM. The magnetization of the speleothem sample calculated by an inversion of isothermal remanent magnetization (IRM) also suggests that magnetic mineral content in the surface layer is higher than the inner layer. This feature was further investigated by low-temperature magnetometry and was suggested that it contains magnetite, maghemite, and goethite. The first-order reversal curve (FORC) measurements and the decomposition of IRM curves show that this speleothem contains a mixture of magnetic minerals with different coercivities and domain states. The contribution from maghemite and goethite to the total magnetization of the grayish surface layer is much higher than the white inner layer. The speleothem retaining magnetically and visually two distinct layers indicates that the depositional environment was shifted when the surface layer was deposited and was likely changed to the oxidative environment.


# Introduction

A typical approach used to unveil the evolution of the geomagnetic field is to extract paleomagnetic signals recorded in geologic materials such as volcanic rocks and sediments. However, obtaining accurate chronology on these geologic archives is not trivial. Age uncertainties on radiometric dating of volcanic rocks typically associate an age error with a few percents (e.g., ~ hundreds of years for ~ 50 ka rock) that make it challenging to depict a precise picture of events. The age models of sediments are often indirect, and the magnetization of sediments lagged behind as much as thousands of years due to magnetization acquisition mechanisms called lock-in depth (Roberts et al., 2013).

Recently, speleothems have been used to overcome these problems because it captures the geomagnetic signals synchronously with the formation of carbonate layers incorporating some magnetic minerals. Also, samples can be dated radiometrically using the Uranium-series dating method. Their structures are not impacted by later diagenesis, consolidation, or deformation after the deposition as compared to sediments. Moreover, the time lag between their crystallization and lock-in of paleomagnetic signals is

considered to be small (e.g., Latham et al., 1979; Morinaga et al., 1989). Thus, several speleothem magnetism studies reported accurate ages of geomagnetic excursions using U/Th-dated speleothems (e.g., Osete et al., 2012; Lascu et al., 2016; Pozzi et al., 2019).

Another advantage of using speleothems to reconstruct paleomagnetism is that it can be used as a recorder of the paleoenvironment employing environmental magnetism approaches (Lascu and Feinberg, 2011). Magnetic minerals deposited on speleothems are derived with the floodwaters into caves and/or drip action through overlying soils. The magnetic minerals in speleothems can, therefore, record regional and global environmental changes such as paleofloods, precipitation, and anthropogenic influences as variations in rock magnetic properties (e.g., Lascu and Feinberg, 2011; Font et al., 2014; Jaqueto et al., 2016; Chen et al., 2019; Feinberg et al., 2020).

Despite the advantages mentioned above, the paleomagnetic signals of speleothems are too weak to reconstruct high-resolution paleomagnetic records by conventional magnetometers (Lascu et al., 2016). Thus, previous studies had to sacrifice temporal resolution that speleothems could potentially offer. Whereas scanning SQUID microscopy (SSM) can image very weak magnetic fields above natural geologic sample with a high spatial resolution of ~ 100 μm (e.g., Lima and Weiss, 2016; Oda et al., 2016), which could likely solve the problem of weak magnetism associated with Speleothem based paleomagnetic studies. To date, only a few preliminary studies addressing the using SSM on speleothems have been reported (e.g., Myre et al., 2019; Feinberg et al., 2020). In this study, we report a result from high-resolution and high sensitivity paleomagnetic and environmental magnetic investigation based on magnetic mapping with an SSM and rock magnetic measurements on a speleothem collected from Tongatapu Island, the Kingdom of Tonga.

# Sample And Methods

A stalagmite sample (AAC) was retrieved from the Anahulu cave in Tongatapu island (21°12'26" S, 175° 05'59" W, Supplementary Figure S1). The AAC sample was first cut perpendicular to its growth direction and then subsampled for different analyses (Figure 1). For SSM measurements, a topmost part of the speleothem was sliced and polished to a thickness of approximately 200 μm. For rock magnetic measurements using a magnetic property measurement system (MPMS) and an alternating gradient force magnetometer (AGM), a small quantity of material was collected from the grayish (close to the surface, AAC-B1, 2, and 3) and white (inner part, AAC-W1, 2, and 3) sections of the speleothem. A powdered sample of the white section of the stalagmite, which is just beneath the greyish layer, was sub-sampled for radiocarbon dating and was graphitized using the method described by Yokoyama et al. (2007) and then measured by a single-stage accelerator mass spectrometry at the Atmosphere and Ocean Research Institute, The University of Tokyo (Yokoyama et al., 2019). The $^{14}C$ age around the boundary between the grayish and white layers of the stalagmite is 10280±110 B.P (Supplementary Figure S2).

The SSM measurements were conducted using an SSM at the Geological Survey of Japan (GSJ), National Institute of Advanced Industrial Science and Technology (AIST) (Kawai et al. 2016; Oda et al. 2016). All measurements were performed with constant parameters described below except a sensor-to-sample distance: scanning steps of x and y axes were 100 μm; speeds of x and y axes were 150 mm/min; delay time before data acquisition was 0.05 s; scanning mode was one-way scanning in the direction of the y-axis. A sensor-to-sample distance was set to be approximately 250 – 350 μm depending on measurement runs. First, natural remanent magnetization (NRM) at alternating field (AF) demagnetization steps of 0, 5, 10, and 30 mT, which was done using an AF demagnetizer equipped with a two-axis tumbler (DEM-95C; Natsuhara Giken Co. Ltd.), was analyzed. Subsequently, isothermal remanent magnetization (IRM) was imparted to the thin section by a DC field of 1.4 T using an electromagnet and was analyzed. Distributions of magnetic moments were calculated from the magnetic field data of IRM by assuming equally spaced magnetic dipoles on 200 μm grids, with upward magnetic moments perpendicular to the thin section using the inversion algorithm of Weiss et al. (2007). Optical images were taken separately with an optical scanner (spatial resolution of 4 μm), which was overlaid with the magnetic image by marking two artificial magnetic dipoles for reference (Oda et al., 2016).

The rock magnetic measurements using an MPMS were conducted using an instrument (MPMS-XL5, Quantum Design) at the Center for Advanced Marine Core Research (CMCR), Kochi University, for analyses mostly relevant to temperature cycles. The sequences of measurement cycles are listed below:

1. ZF-cycling curve: imparting saturation isothermal remanent magnetization (SIRM) by a magnetic field of 5 T at room temperature (300 K); measuring a remanence continuously while cooling from 300 K to 8 K and warming back to 300 K in zero field
2. FC curve: cooling from 300 K to 8 K in a magnetic field of 5 T; measuring a remanence in zero field during warming from 8 to 300 K.
3. ZFC curve: cooling from 300 K to 8 K in zero field; imparting SIRM in a field of 5 T at 8 K; measuring a remanence in zero field during warming from 8 to 300 K.
4. 400 K thermoremanent magnetization (TRM) and ZF-cycling: imparting TRM by heating to 400K and cooling to 300K in a magnetic field of 300 mT, according to Lascu and Feinberg (2011) and Guyodo et al. (2006); measuring a remanence with the same protocol of ZF-cycling.
5. 400 K thermal demagnetization (ThD) and ZF-cycling: ThD by heating to 400 K and cooling to 300K in zero field; imparting IRM with a magnetic field of 300 mT at 300 K; measuring a remanence with the same protocol of ZF-cycling.

Note that a difference between the two measurements of 4 and 5 was used to diagnose the presence of goethite (Lascu and Feinberg, 2011). Moreover, IRM acquisition curves were obtained at 60 steps on a logarithmic scale up to 5 T at room temperature. IRM acquisition results were decomposed by Max UnMix software (Maxbauer et al., 2016).

The rock magnetic measurements using an AGM were conducted using an instrument (PMC MicroMag 2900 AGM; Lake Shore Cryotronics, Inc.) at GSJ, AIST, for hysteresis and first-order reversal curve (FORC)

analyses. Hysteresis data were processed using the software HystLab developed by Paterson et al. (2018), and FORC measurement data were analyzed using the software FORCinel developed by Harrison and Feinberg (2008).

## Results

# SSM measurements

Optical (Fig. 2a) and magnetic images (Fig. 2b) were first taken for NRM before AF demagnetization, and an overlay image was produced (Fig. 2c) for SSM measurements. The grayish surface layer observed in the optical image shows positive magnetic anomalies of approximately 0.15 nT (standard deviation: ~0.48 nT) on average, whereas weak negative anomalies (average ~ -0.58 nT, standard deviation: ~0.26 nT) were presented in the white layer (Fig. 2d).

After demagnetization at 5 mT, a magnetic image of NRM for the white inner layer shows weak positive anomalies of about 0.09 nT (Supplementary Figures S3b and S3c), which is different from the values obtained from NRM. It is possible that the secondary magnetization acquired after speleothem formation was removed by AF demagnetization at 5 mT. Even after demagnetization at 10 mT and 30 mT, the white inner layer shows weak positive anomalies (Supplementary Figures S3b and S3c). The cross-sectional diagrams along the centerline of the speleothem growth axis visualize well the change of magnetic field values through AF demagnetization (Supplementary Figures S4b, d, f, and h). The magnetic field values of these anomalies are consistent with previously reported values for speleothems in Lascu and Feinberg (2011). Viscous magnetic overprints acquired after speleothem formation can be removed in the laboratory by magnetic cleaning involving partial alternating field (AF) demagnetization using peak fields from 5–10 mT (e.g., Latham et al., 1987; Morinaga et al., 1989) to 30 mT (Openshaw et al., 1997).

Magnetic images of IRM indicate that magnetic field values above the black layer are much higher than those above the white layer (Figs. 2e, 2f, and 2 g). In order to compare magnetizations of the two layers, magnetic moments of dipole magnetic sources on uniform grids of 0.2 mm × 0.2 mm were calculated in accordance with Weiss et al. (2007). The results indicate that magnetic moment values above the black layer are higher than those above the white layer (Fig. 2h and 2i). This could be suggested that the concentration of magnetic minerals is higher in the grayish layer than the white layer. The above-described exercises demonstrated that SSM could image very weak magnetic field differences induced from differences in laminated structures of a speleothem at the submillimeter scale.

# Magnetic mineralogy with low temperature magnetometry

Results from low-temperature magnetometry experiments for samples AAC-B and AAC-W are shown in Figs. 4 and 5. In general, inflection points around 120 K attributed to the Verwey transition, a characteristic feature for magnetite, are found. However, although the degree of inflections found in this study for the white layer shows general agreement, the grey layers seem not identical from the feature expected to be found for stoichiometric magnetite. In the ZF-cycling and FC/ZFC curves of AAC-W1

(Figs. 4b and 4d), the transition can be observed clearly, while in the corresponding diagrams of AAC-B1 (Figs. 4a and 4c), the transition is not clear. Similarly, the ZF-cycling curve of TRM at 400 K and that after thermal demagnetization (ThD) at 400 K for AAC-W2 (Figs. 5b and 5d) show the inflection points corresponding to the Verwey transition, whereas those for AAC-B2 (Figs. 5a and 5c) do not show this transition. The clear transitions of the white inner layers suggested that their main magnetic carrier is relatively stoichiometric magnetite. In contrast, the vague or absence of the Verwey transition for the grayish surface layers is considered as the result of the oxidation of magnetite. Namely, as the surface of magnetite is oxidized to maghemite, the magnetization changes at the Verwey transition becomes smaller, and the transition is broadened and shifted to a lower temperature (Özdemir and Dunlop, 2010).

It is noteworthy that a warming curve of the ZF-cycling for grayish surface (AAC-B2) exhibits a decreasing trend with increasing temperatures (red curve; Fig. 4a). Furthermore, the FC curve of AAC-B1 (Fig. 4c) is separate from the ZFC curve independent of the Verwey transition. These features are similar to those for the speleothems with the presence of goethite (e.g., Lascu and Feinberg, 2011; Strauss et al., 2013; Jaqueto et al., 2016). Moreover, the difference between the ZF-cycling curves of TRM and ThD for AAC-B2 is non-zero at 300K and slightly increases during while cooling steps (blue curve; Fig. 5e), which also suggests the presence of goethite (Lascu and Feinberg, 2011). In contrast, AAC-W1 does not exhibit the features indicative of goethite clearly for ZF-cycling (Fig. 4b) and FC/ZFC curves (Fig. 4d). Further, the difference between the ZF-cycling curves of TRM and ThD for AAC-W3 is zero at 300K and shows a significant increase around Verwey transition while cooling (Fig. 5f). This might be evidence of the presence of magnetite/maghemite but not of goethite. In summary, relatively stoichiometric magnetite is likely the main magnetic carrier for the white inner layers, whereas this is not the case for the grayish surface layers. In contrast, goethite is probably included in the grayish surface layers, that is not apparent in the white inner layers.

# Hysteresis and domain state diagnosis using FORC

Hysteresis loops are illustrated for the samples collected from the surface grey layer and the inner white layer (Figs. 3a and 3b). The saturation magnetization (Ms) of the surface layer ($3.79 \times 10^{-4}$ $Am^2/kg$) was about four times higher than that of the inner layer ($8.44 \times 10^{-5}$ $Am^2/kg$). This is consistent with the SSM measurements, and we suggest that higher concentrations of magnetic minerals contained in the surface layer than in the inner layer. By contrast, coercivity (Hc) of the surface layer (6.2 mT), on the other hand, was lower than that of the inner layer (12.5 mT).

FORC diagrams of the grayish surface layer (AAC-B3; Figs. 3c) and inner white layer (AAC-W3; Fig. 3d) show the existence of central-ridges around the Bu axis. This may be a typical character of non-interacting single-domain (SD) particles, which could possibly be originated from magnetotactic bacteria (Roberts et al., 2014). Both diagrams also show a multi-domain (MD)-like horizontal spreads, which are similar to the results reported by Harrison et al. (2018). In addition, the FORC diagram of the grayish layer shows a diagonal distribution extending to lower-right between the Bu and Bc axis (Fig. 3c) which is similar to the results on vortex state (pseudo-single-domain) particles (Zhao et al., 2017) or/and

“randomly packed single domain particles” (Harrison et al., 2019). These magnetic components are also similar to those reported for speleothems by Jaqueto et al. (2016). Hence, we posit that the speleothem in this study contains both SD and MD magnetite, at a minimum.

# Identification of coercivity components using IRM acquisition curves

Analytical results of the IRM acquisition curves by the Max UnMix software (Maxbauer et al., 2016) suggest that the grayish layer (AAC-B1) and white layer (AAC-W1) consist of four coercivity components (Figs. 4e and 4f). Both layers have four similar main components: the very-low-coercivity component (Comp-1), the low-coercivity component (Comp-2), the intermediate-coercivity component (Comp-3), and the high-coercivity component (Comp-4: $B_h$ ~1600–2000 mT). Acquisition fields ($B_h$) and dispersion parameter (DP) of each component are similar to those reported for sediments and speleothems (e.g., Yamazaki, 2009; Abrajevitch and Kodama, 2011; Font et al., 2014; and Jaqueto et al., 2016): Comp-1 ($B_h$: ~14–16 mT, DP: ~0.44–0.46) represents a mixture of magnetite and maghemite; Comp-2 ($B_h$: ~37–42 mT, DP: ~0.23) and Comp-3 ($B_h$: ~75–97 mT, DP: ~0.14–0.15) has low coercivities and relatively narrow DPs, which suggest the presence of biogenic magnetite; Comp-4 ($B_h$: ~1600–2000 mT, DP: ~0.38–0.68) represents the presence of goethite, but DP of AAC-W1 is inconsistent with those reported for goethite (e.g., Abrajevitch and Kodama, 2011; Font et al., 2014; and Jaqueto et al., 2016). It is thought that the grayish surface layer should contain goethite, but the white inner layer does not obviously.

## Discussion

# Magnetic minerals in this speleothem

Magnetic mappings of the speleothem from the stalagmite of Anahulu cave with the submillimeter scale with SSM (Figs. 2a, 2b, and 2c) clearly showed a difference in the magnetization distributions between the grayish surface layer and the white inner layer (Figs. 2d, 2e, and 2f). A series of rock magnetic results suggest that the main magnetic remanence carriers in the speleothem studied are magnetite, maghemite, and goethite. Similar results have been obtained in other stalagmites (e.g., Lascu and Feinberg, 2011; Strauss et al., 2013; and Jaqueto et al., 2016).

The results of low-temperature magnetometry suggest that the magnetite in the grayish surface layer could have been partially oxidized to goethite and/or maghemite (Figs. 4a, 4c, 5a, 5c, and 5e). Meanwhile, the main magnetic mineral in the white surface layer is magnetite, and the presence of goethite is not clear (Figs. 4b, 4d, 5b, and 5d). This result consistent with the analyses of IRM acquisitions (Fig. 4e and 4f). Meanwhile, DP shows inconsistent values for Comp-1, 2, and 3 (~ 0.44–0.46, ~ 0.23, and ~ 0.14–0.15, respectively). It suggests that each magnetic component have different characteristics in terms of grain size and composition due to the variability of the physical and chemical processes (Egli, 2004). This is also supported by reading of FORC diagrams, which suggest that the speleothem in this study contains SD and MD magnetite.

Thus, the assemblage of magnetic minerals in the grayish surface layer comprises a mixture of magnetite, maghemite, and goethite. In contrast, the assemblage of magnetic minerals in the white inner layer is dominated by magnetite and small quantities of goethite. We suggest that the depositional condition of the surface layer is different from that of the inner layer since the latter.

# Environmental magnetic implication

Results obtained from the present study demonstrate that different magnetic properties can be detected clearly between the two layers using SSM. Concentrations of magnetic minerals are higher in the black layer, whereas much smaller in the white layer. The type of magnetic minerals contained in the two layers also can be distinguished. According to Lascu and Feinberg (2011), the deposition rate of detrital magnetic minerals onto the speleothem surface is controlled by precipitation, flood frequency, and soil in the surface layer situated strata above. We thus may potentially be attributed depositional mechanism of black and white layers to changes in ambient environments. Recording of distinct several colored layers would be expected if the change observed in this study occurred over time as a result of frequent events such as extreme climate changes, including floods and/or tsunamis (e.g., Denniston and Luetscher, 2017; Feinberg et al., 2020). However, no recurrence of distinct layers was found, and only a single black layer on the surface of the speleothem has existed. This might suggest that the black layer was formed as the consequence of the relatively short-lived unique event that happened during the last ca. 10,000 years. The distinct grey to black color on the white calcium carbonate speleothem also is suspected that the origin of this color is coming from sediments dominated by non-carbonate minerals. Tongatapu island consists mainly of limestone and overlaid two soil layers from andesitic volcanic ash, which is estimated to be 20,000 and 5,000 years old (e.g., Cowie, 1980; Spennmenn, 1997; Manu et al., 2007). Magnetic minerals in soils of Ha' apai, Kingdom of Tonga consist mainly of goethite (Childs and Willson, 1993). Furthermore, typically soil containing volcanic ash is acidic; thus, magnetite in the soil could oxidize to maghemite (Taylor and Schwertmann, 1974). Therefore, it is considered that the black layers are mainly originated from volcanic eruptions that occurred neighboring islands.

The other possible scenario would be the potential influence of human activities. As the previous studies suggested, soil magnetic and archaeomagnetic studies can indicate that an increase in fire and organic carbon supply from human activities could lead to the transformation of into ferrimagnetic mineral (e.g., Marmet et al., 1999; Hanesch et al., 2006; Fassbinder, 2015). The results observed from this study also reveal similar magnetic properties that would point out the influence of fire. Future work, such as U/Th dating, is needed to discuss the processes affecting the magnetism of speleothems.

# Conclusion

We successfully performed SSM on a speleothem collected from a cave on Tongatapu Island in combination with a series of rock magnetic measurements. We could observe magnetic images of the speleothem at the submillimeter scale with SSM and detected the difference in the magnetic field maps associated with the laminated growth structure distinguishing between surface grayish to black colored and inner white-colored layers. Further, rock magnetic measurements showed that: 1) the magnetic

mineral content in the grayish surface layer is higher relative to that in the white inner layer; 2) the speleothem in this study contains several magnetic minerals (magnetite, maghemite, and goethite) with different domain states; and, 3) the contribution of maghemite and goethite is much larger in the surface layer than in the inner layer. The magnetic mineralogy of the surface layer different from that of the inner layer could have occurred due to the change of the depositional environment of the magnetic minerals in the speleothem to the oxidative condition.

# Declarations

### Ethics approval and consent to participate

Not applicable.

### Consent for publication

Not applicable.

### Availability of data and materials

The datasets used and/or analyzed during the current study are available from the corresponding author upon reasonable request.

### Competing interests

The authors declare that they have no competing interests.


### Funding

Part of this research was supported by a grant from the Japan Society for the Promotion of Science (JSPS) KAKENHI (JP17H01168) and a Grant-in-Aid for JSPS Fellows DC1 (JP18J21630).


### Authors' contributions

NF carried out sample preparations, measurements with SQUID microscope and AGM, data analyses, and drafted the manuscript. HO and Y. Yokoyama conceived the study, participated in its design and coordination, and helped draft the manuscript. HO maintained the SQUID microscope and developed software for the data analyses. GC organized the fieldwork and collecting the samples. Y. Yamamoto maintained the MPMS and helped with its measurements. All authors read and approved the final manuscript.


### Acknowledgments

We thank Mr. Nivaleti Melekiola (the former Lapaha District Officer) and Mr. Shane Egan (Tonga Maritime Museum) for their assistance in sampling. We also thank Ms. Ayako Katayama for assistance with the

sample measurements using the scanning SQUID microscope. A part of this study conducted by NF was carried out as a research assistant in AIST.

# Abbreviations

NRM: Natural Remanent Magnetization

IRM: Isothermal Remanent Magnetization

TRM: Thermal Remanent Magnetization

FC: Field Cycling

ZFC: Zero Field Cycling

ThD: Thermal Demagnetization

SSM: Scanning SQUID Microscope

GSJ: Geological Survey of Japan

AIST: National Advanced Industrial Science and Technology

$B_h$: the mean coercivity of an individual grain population

DP: the dispersion parameter of an individual grain population

# References

1. Abrajevitch A, Kodama K (2011) Diagenetic sensitivity of paleoenvironmental proxies: A rock magnetic study of Australian continental margin sediments: DIAGENESIS. Geochem Geophys Geosyst 12:. https://doi.org/10.1029/2010GC003481

2. Bronk Ramsey C (2009) Bayesian Analysis of Radiocarbon Dates. Radiocarbon 51:337–360. https://doi.org/10.1017/S0033822200033865

3. Chen Q, Zhang TW, Wang YT, Zhao JX, Feng YX, Liao W, Wang W, Yang XQ (2019) Magnetism Signals in a Stalagmite From Southern China and Reconstruction of Paleorainfall During the Interglacial-Glacial Transition. Geophys Res Lett 46:6918–6925. https://doi.org/10.1029/2019GL082204

4. Childs CW, Wilson AD (1983) Iron oxide minerals in soils of the Ha'apai group, Kingdom of Tonga. Soil Res 21:489–503. https://doi.org/10.1071/sr9830489

5. Cowie JD (1980) Soils from Andesitic Tephra and their variability, Tongatapu, Kingdom of Tonga. Soil

Res 18:273–284. https://doi.org/10.1071/sr9800273

6. Denniston RF, Luetscher M (2017) Speleothems as high-resolution paleoflood archives. Quat Sci Rev 170:1–13. https://doi.org/10.1016/j.quascirev.2017.05.006

7. Egli R (2004) Characterization of Individual Rock Magnetic Components by Analysis of Remanence Curves, 1. Unmixing Natural Sediments. Studia Geophys Geodaetica 48:391–446. https://doi.org/10.1023/B:SGEG.0000020839.45304.6d

8. Fassbinder JWE (2015) Seeing beneath the farmland, steppe and desert soil: magnetic prospecting and soil magnetism. J Archaeol Sci 56:85–95. https://doi.org/10.1016/j.jas.2015.02.023

9. Feinberg JM, Lascu I, Lima EA, Weiss BP, Dorale JA, Alexander EC, Edwards RL (2020) Magnetic detection of paleoflood layers in stalagmites and implications for historical land use changes. Earth Planet Sci Lett 530:115946. https://doi.org/10.1016/j.epsl.2019.115946

10. Font E, Veiga-Pires C, Pozo M, Carvallo C, de Siqueira Neto AC, Camps P, Fabre S, Mirão J (2014) Magnetic fingerprint of southern Portuguese speleothems and implications for paleomagnetism and environmental magnetism: Magnetic fingerprint of speleothems. J Geophys Res [Solid Earth] 119:7993–8020. https://doi.org/10.1002/2014JB011381

11. Gibbs HS (1976) Soils of Tongatapu Island, Tonga. N.Z. soil survey report

12. Guyodo Y, LaPara TM, Anschutz AJ, Penn RL, Banerjee SK, Geiss CE, Zanner W (2006) Rock magnetic, chemical and bacterial community analysis of a modern soil from Nebraska. Earth Planet Sci Lett 251:168–178. https://doi.org/10.1016/j.epsl.2006.09.005

13. Hanesch M, Stanjek H, Petersen N (2006) Thermomagnetic measurements of soil iron minerals: the role of organic carbon. Geophys J Int 165:53–61. https://doi.org/10.1111/j.1365-246X.2006.02933.x

14. Harrison RJ, Feinberg JM (2008) FORCinel: An improved algorithm for calculating first-order reversal curve distributions using locally weighted regression smoothing: FORCINEL ALGORITHM. Geochem Geophys Geosyst 9:. https://doi.org/10.1029/2008GC001987

15. Harrison RJ, Muraszko J, Heslop D, Lascu I, Muxworthy AR, Roberts AP (2018) An Improved Algorithm for Unmixing First-Order Reversal Curve Diagrams Using Principal Component Analysis. Geochem Geophys Geosyst 19:1595–1610. https://doi.org/10.1029/2018GC007511

16. Harrison RJ, Zhao X, Hu P, Sato T, Heslop D, Muxworthy AR, Oda H, Kuppili VSC, Roberts AP (2019) Simulation of Remanent, Transient, and Induced FORC Diagrams for Interacting Particles With Uniaxial,

Cubic, and Hexagonal Anisotropy. J Geophys Res [Solid Earth] 124:12404–12429. https://doi.org/10.1029/2019JB018050

17. Hogg AG, Hua Q, Blackwell PG, Niu M, Buck CE, Guilderson TP, Heaton TJ, Palmer JG, Reimer PJ, Reimer RW, Turney CSM, Zimmerman SRH (2013) SHCal13 Southern Hemisphere Calibration, 0–50,000 Years cal BP. Radiocarbon 55:1889–1903. https://doi.org/10.2458/azu_js_rc.55.16783

18. Jaqueto P, Trindade RIF, Hartmann GA, Novello VF, Cruz FW, Karmann I, Strauss BE, Feinberg JM (2016) Linking speleothem and soil magnetism in the Pau d'Alho cave (central South America). J Geophys Res [Solid Earth] 121:7024–7039. https://doi.org/10.1002/2016JB013541

19. Lascu I, Feinberg JM (2011) Speleothem magnetism. Quat Sci Rev 30:3306–3320. https://doi.org/10.1016/j.quascirev.2011.08.004

20. Lascu I, Feinberg JM, Dorale JA, Cheng H, Lawrence Edwards R (2016) Age of the Laschamp excursion determined by U-Th dating of a speleothem geomagnetic record from North America. Geology 44:139–142. https://doi.org/10.1130/G37490.1

21. Latham AG, Schwarcz HP, Ford DC, Pearce GW (1979) Palaeomagnetism of stalagmite deposits. Nature 280:383–385. https://doi.org/10.1038/280383a0

22. Lima EA, Weiss BP (2016) Ultra-high sensitivity moment magnetometry of geological samples using magnetic microscopy: ULTRA-SENSITIVE MOMENT MAGNETOMETRY. Geochem Geophys Geosyst 17:3754–3774. https://doi.org/10.1002/2016GC006487

23. Manu V, Whitbread A, Blair N, Blair G (2014) Carbon status and structural stability of soils from differing land use systems in the Kingdom of Tonga. Soil Use Manage 30:517–523. https://doi.org/10.1111/sum.12135

24. Marmet E, Bina M, Fedoroff N, Tabbagh A (1999) Relationships between human activity and the magnetic properties of soils: a case study in the medieval site of Roissy-en-France. Archaeological Prospection 6:161–170

25. Maxbauer DP, Feinberg JM, Fox DL (2016) MAX UnMix: A web application for unmixing magnetic coercivity distributions. Comput Geosci 95:140–145. https://doi.org/10.1016/j.cageo.2016.07.009

26. Morinaga H, Inokuchi H, Yaskawa K (1989) Palaeomagnetism of stalagmites (speleothems) in SW Japan. Geophys J Int 96:519–528. https://doi.org/10.1111/j.1365-246X.1989.tb06011.x

27. Myre JM, Lascu I, Lima EA, Feinberg JM, Saar MO, Weiss BP (2019) Using TNT-NN to unlock the fast

full spatial inversion of large magnetic microscopy data sets. Earth Planets Space 71:14. https://doi.org/10.1186/s40623-019-0988-8

28. Oda H, Kawai J, Miyamoto M, Miyagi I, Sato M, Noguchi A, Yamamoto Y, Fujihira J-I, Natsuhara N, Aramaki Y, Masuda T, Xuan C (2016) Scanning SQUID microscope system for geological samples: system integration and initial evaluation. Earth Planets Space 68:179. https://doi.org/10.1186/s40623-016-0549-3

29. Osete M-L, Martín-Chivelet J, Rossi C, Edwards RL, Egli R, Muñoz-García MB, Wang X, Pavón-Carrasco FJ, Heller F (2012) The Blake geomagnetic excursion recorded in a radiometrically dated speleothem. Earth Planet Sci Lett 353-354:173–181. https://doi.org/10.1016/j.epsl.2012.07.041

30. Özdemir Ö, Dunlop DJ (2010) Hallmarks of maghemitization in low-temperature remanence cycling of partially oxidized magnetite nanoparticles. J Geophys Res 115:430. https://doi.org/10.1029/2009JB006756

31. Paterson GA, Zhao X, Jackson M, Heslop D (2018) Measuring, Processing, and Analyzing Hysteresis Data. Geochem Geophys Geosyst 19:1925–1945. https://doi.org/10.1029/2018GC007620

32. Pozzi J-P, Rousseau L, Falguères C, Mahieux G, Deschamps P, Shao Q, Kachi D, Bahain J-J, Tozzi C (2019) U-Th dated speleothem recorded geomagnetic excursions in the Lower Brunhes. Sci Rep 9:1114. https://doi.org/10.1038/s41598-018-38350-4

33. Roberts AP, Almeida TP, Church NS, Harrison RJ, Heslop D, Li Y, Li J, Muxworthy AR, Williams W, Zhao X (2017) Resolving the Origin of Pseudo-Single Domain Magnetic Behavior: Origin of PSD Behavior. J Geophys Res [Solid Earth] 122:9534–9558. https://doi.org/10.1002/2017JB014860

34. Roberts AP, Heslop D, Zhao X, Pike CR (2014) Understanding fine magnetic particle systems through use of first-order reversal curve diagrams. Rev Geophys 52:2014RG000462. https://doi.org/10.1002/2014RG000462

35. Roberts AP, Pike CR, Verosub KL (2000) First-order reversal curve diagrams: A new tool for characterizing the magnetic properties of natural samples. J Geophys Res 105:28461–28475. https://doi.org/10.1029/2000JB900326

36. Roberts AP, Tauxe L, Heslop D (2013) Magnetic paleointensity stratigraphy and high-resolution Quaternary geochronology: successes and future challenges. Quat Sci Rev 61:1–16. https://doi.org/10.1016/j.quascirev.2012.10.036

37. Spennemann DHR (1997) A Holocene sea-level history for Tongatapu, Kingdom of Tonga. Coastal

and Environmental geoscience studies of the Southwest Pacific Islands SOPA Technical Bulletin 9:115–152

38. Strauss BE, Strehlau JH, Lascu I, Dorale JA, Penn RL, Feinberg JM (2013) The origin of magnetic remanence in stalagmites: Observations from electron microscopy and rock magnetism. Geochem Geophys Geosyst 14:5006–5025. https://doi.org/10.1002/2013GC004950

39. Taylor RM, Schwertmann U (1974) Maghemite in soils and its origin: II. Maghemite syntheses at ambient temperature and pH 7. Clay Miner 10:299–310. https://doi.org/10.1180/claymin.1974.010.4.08

40. Trindade RIF, Jaqueto P, Terra-Nova F, Brandt D, Hartmann GA, Feinberg JM, Strauss BE, Novello VF, Cruz FW, Karmann I, Cheng H, Edwards RL (2018) Speleothem record of geomagnetic South Atlantic Anomaly recurrence. Proc Natl Acad Sci U S A 115:13198–13203. https://doi.org/10.1073/pnas.1809197115

41. Weiss BP, Lima EA, Fong LE, Baudenbacher FJ (2007) Paleomagnetic analysis using SQUID microscopy. J Geophys Res 112:11715. https://doi.org/10.1029/2007JB004940

42. Yamazaki T (2009) Environmental magnetism of Pleistocene sediments in the North Pacific and Ontong-Java Plateau: Temporal variations of detrital and biogenic components: ENVIRONMENTAL MAGNETISM OF PACIFIC SEDIMENTS. Geochem Geophys Geosyst 10:. https://doi.org/10.1029/2009GC002413

43. Yokoyama Y, Koizumi M, Matsuzaki H, Miyairi Y, Ohkouchi N (2010) Developing Ultra Small-Scale Radiocarbon Sample Measurement at the University of Tokyo. Radiocarbon 52:310–318. https://doi.org/10.1017/S0033822200045355

44. Yokoyama Y, Miyairi Y, Matsuzaki H, Tsunomori F (2007) Relation between acid dissolution time in the vacuum test tube and time required for graphitization for AMS target preparation. Nucl Instrum Methods Phys Res B 259:330–334. https://doi.org/10.1016/j.nimb.2007.01.176

45. Zhao X, Roberts AP, Heslop D, Paterson GA, Li Y, Li J (2017) Magnetic domain state diagnosis using hysteresis reversal curves: Magnetic Domain State Diagnosis by FORCs. J Geophys Res [Solid Earth] 122:4767–4789. https://doi.org/10.1002/2016JB013683

# Figures

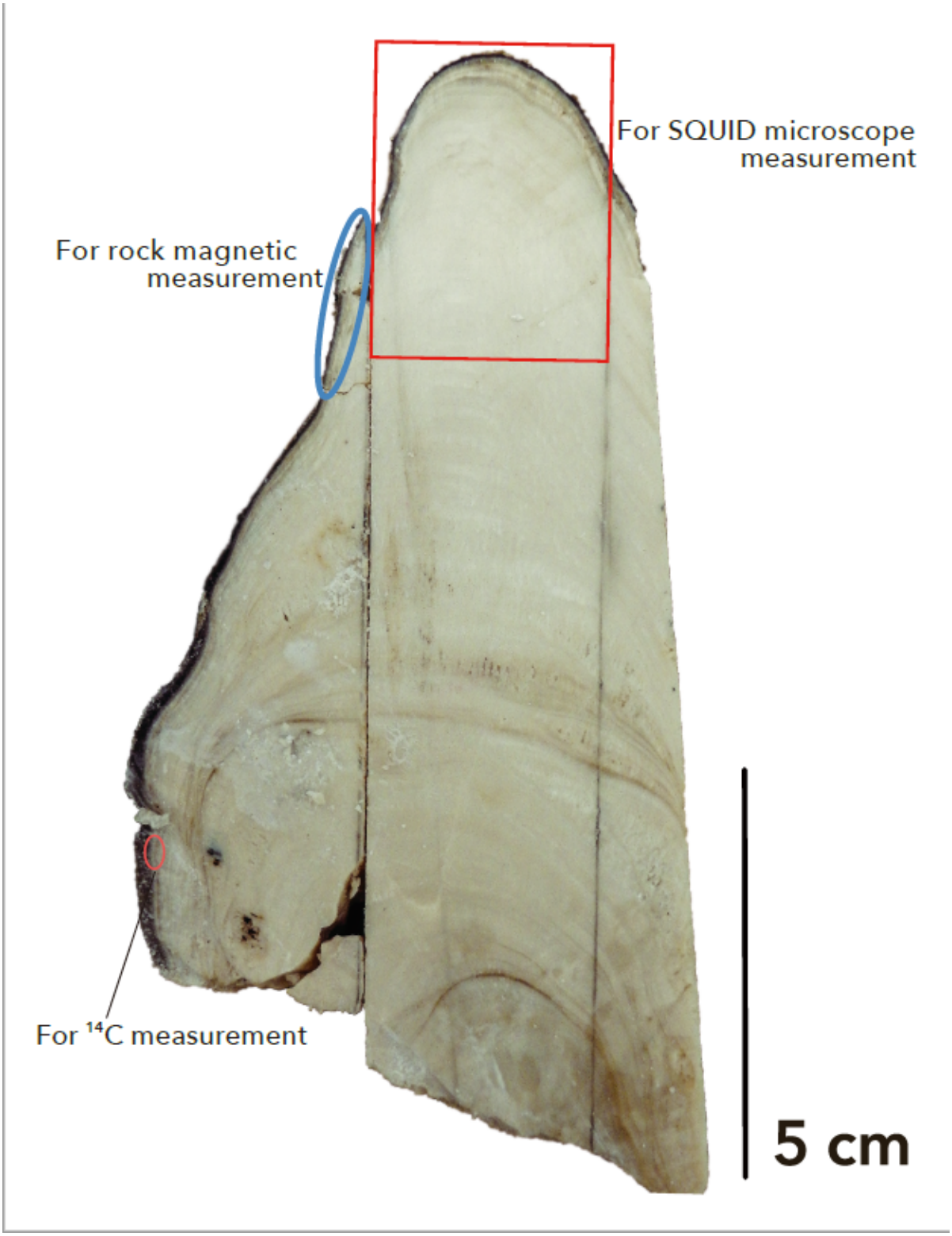


**Figure 1**

Photo of a half-split sample of a speleothem used for SSM and rock magnetic measurements, and 14C dating.

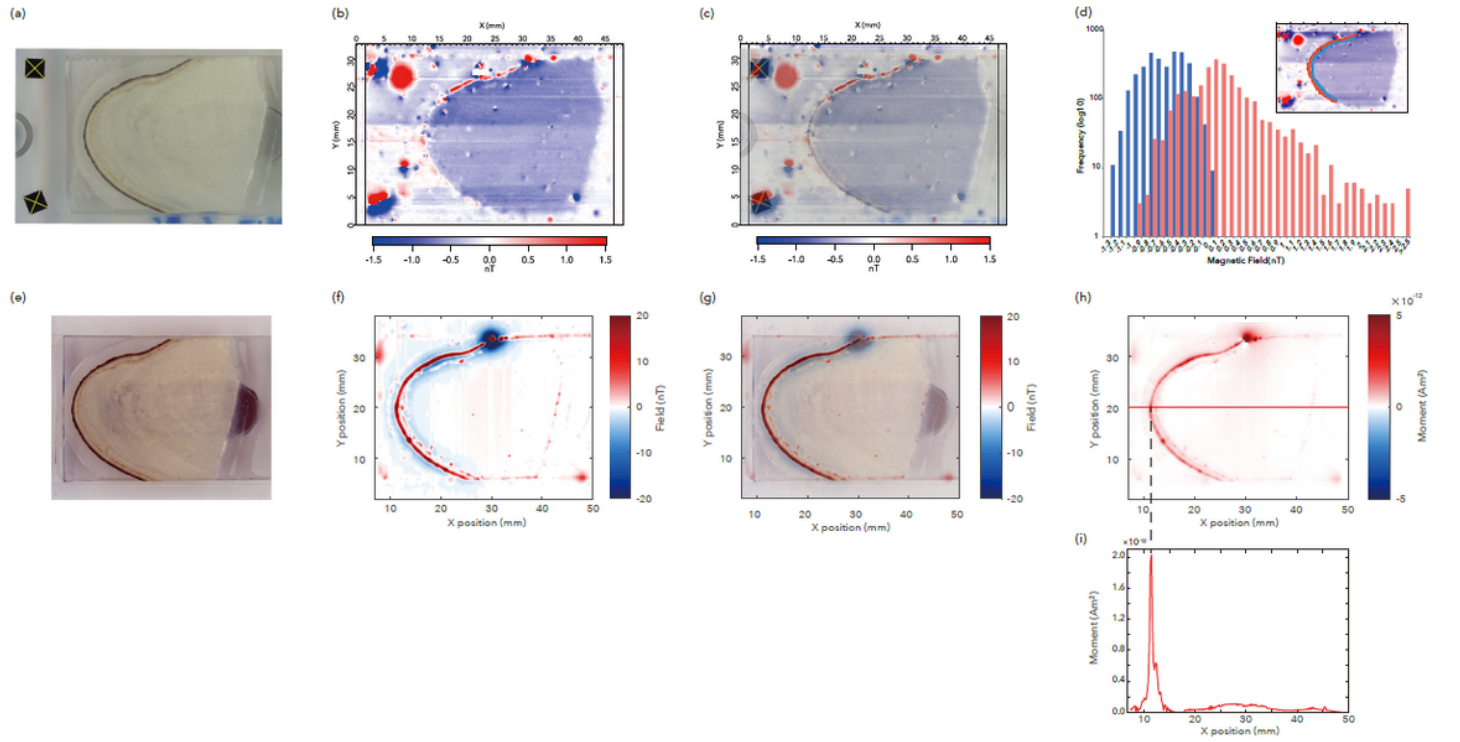


## Figure 2

Optical and magnetic images of NRM and IRM, and their analyses. (a) Optical image, (b) magnetic image of NRM, and (c) optical image overlaid on magnetic image of NRM. (d) Distribution of magnetic field within the highly magnetic layer next to the surface and the layer slightly inside with less magnetic feature. Each dataset was selected according to the region shown in the inset figure on the upper-right; i.e., red and blue correspond to the magnetic and less magnetic areas, respectively. (e) Optical image (contrast has been changed from Fig. 2a for better visibility of the colored surface layers), (f) magnetic image of IRM (1.4 T), and (g) optical image overlaid on a magnetic image of IRM (1.4 T). (h) Magnetic moment distribution of IRM image calculated on 0.2 mm × 0.2 mm grid points from the magnetic field in Fig. 2(f). Magnetic moment distributions were calculated, according to Weiss et al. (2007). (i) Line profile along a horizontal line in Fig. 2(h) at 20.1 mm of Y position. The range of gray shade is the same as the range of a light green square in Fig. 2(h).

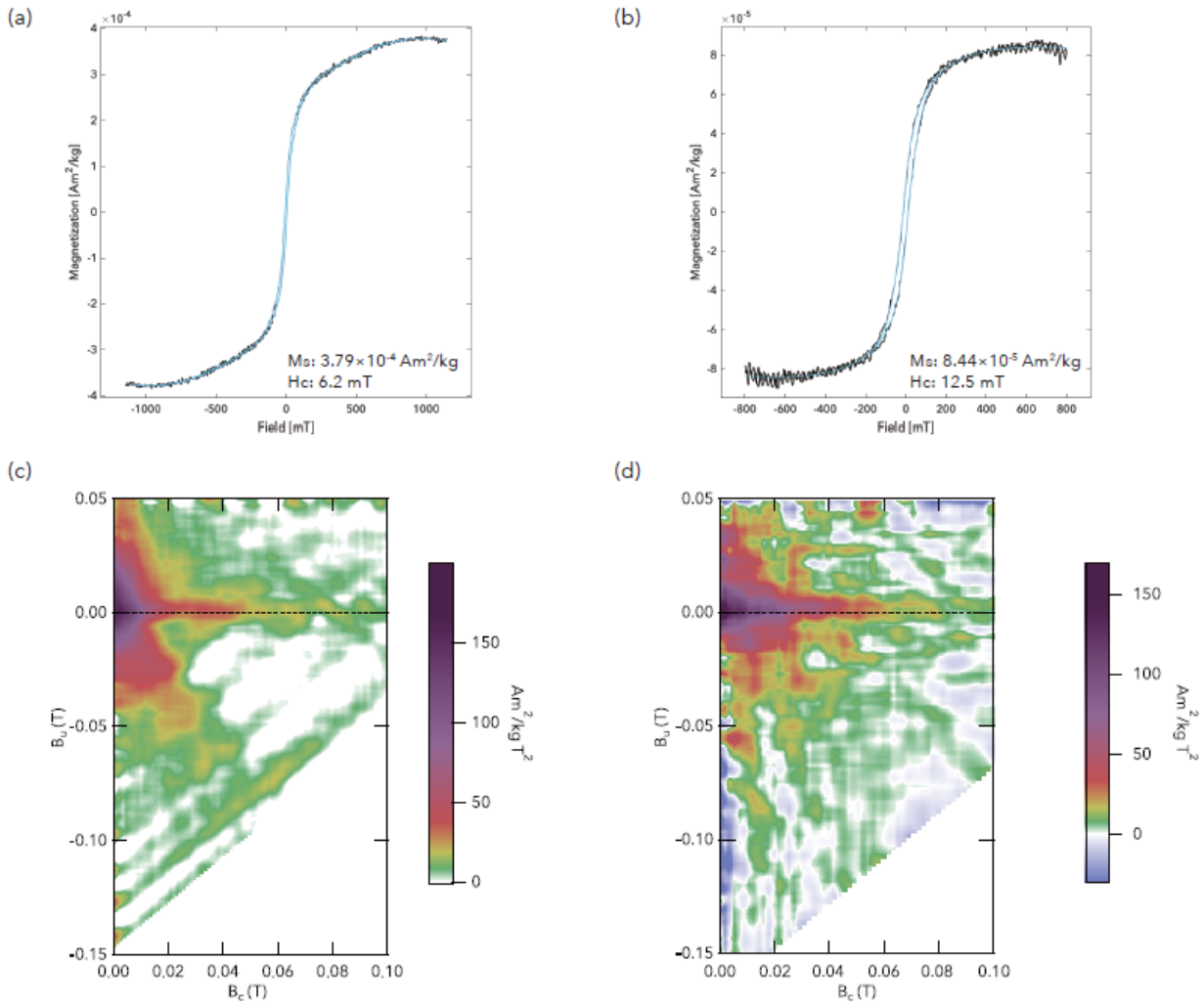


## Figure 3

Results of measurements with AGM for samples from the grayish section (AAC-B1) and white section (AAC-W1). Hysteresis loops of (a) AAC-B1 and (b) AAC-W1, and FORC diagrams of (c) AAC-B1 and (d) AAC-W1.

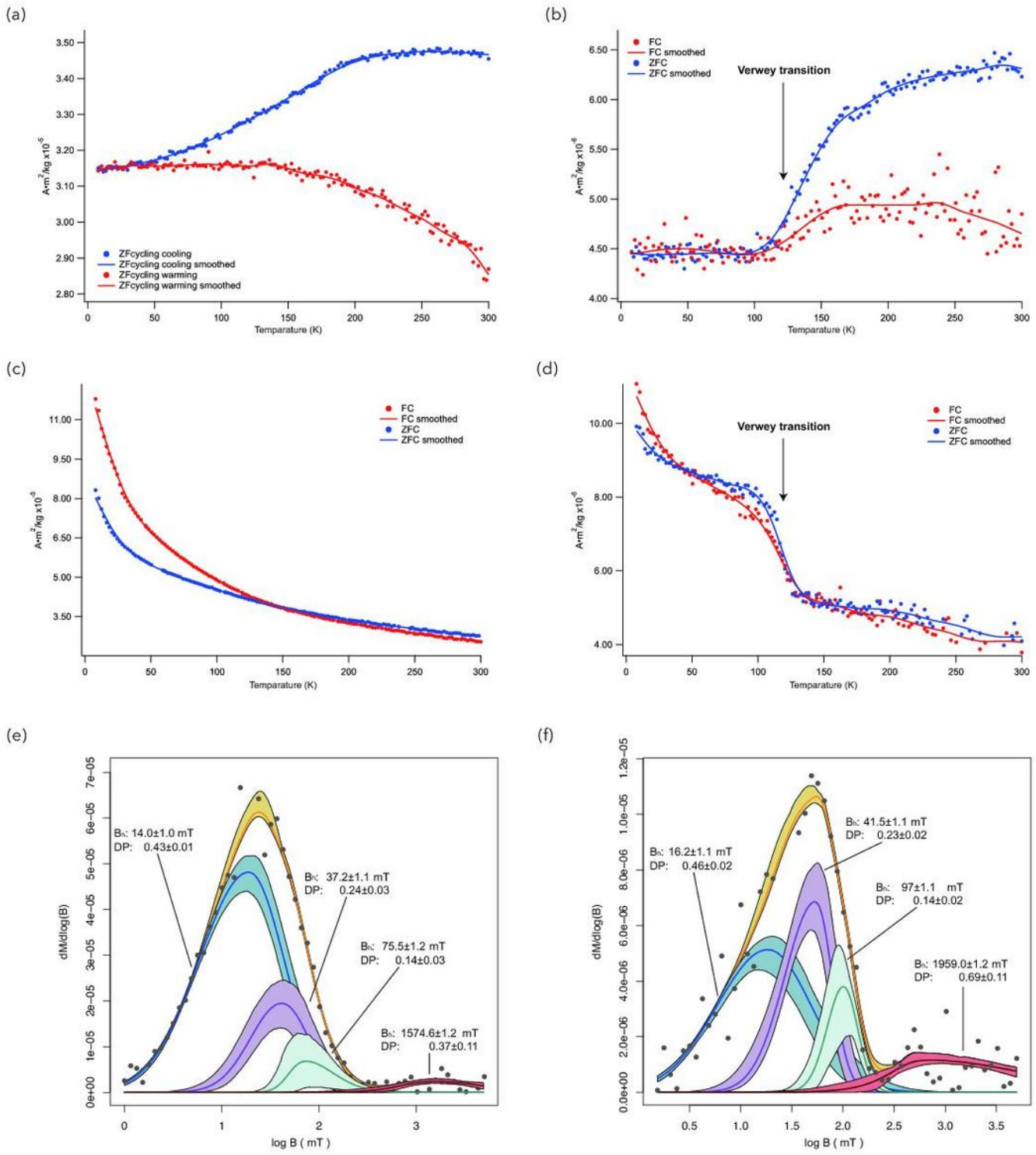


## Figure 4

ZF-cycling curves of (a) AAC-B1 (the grayish surface layer) and (b) AAC-W1 (the white inner layer); FC/ZFC curves of (c) AAC-B2 and (d) AAC-W2; and Results of IRM acquisition curves analyses using MAX UnMix (Maxbauer et al. 2016) of (e) AAC-B1 and (f) AAC-W2. Bh and DP are the mean coercivity and the dispersion parameter (given by one standard deviation) of an individual grain population assuming a Gaussian distribution in log space, respectively.

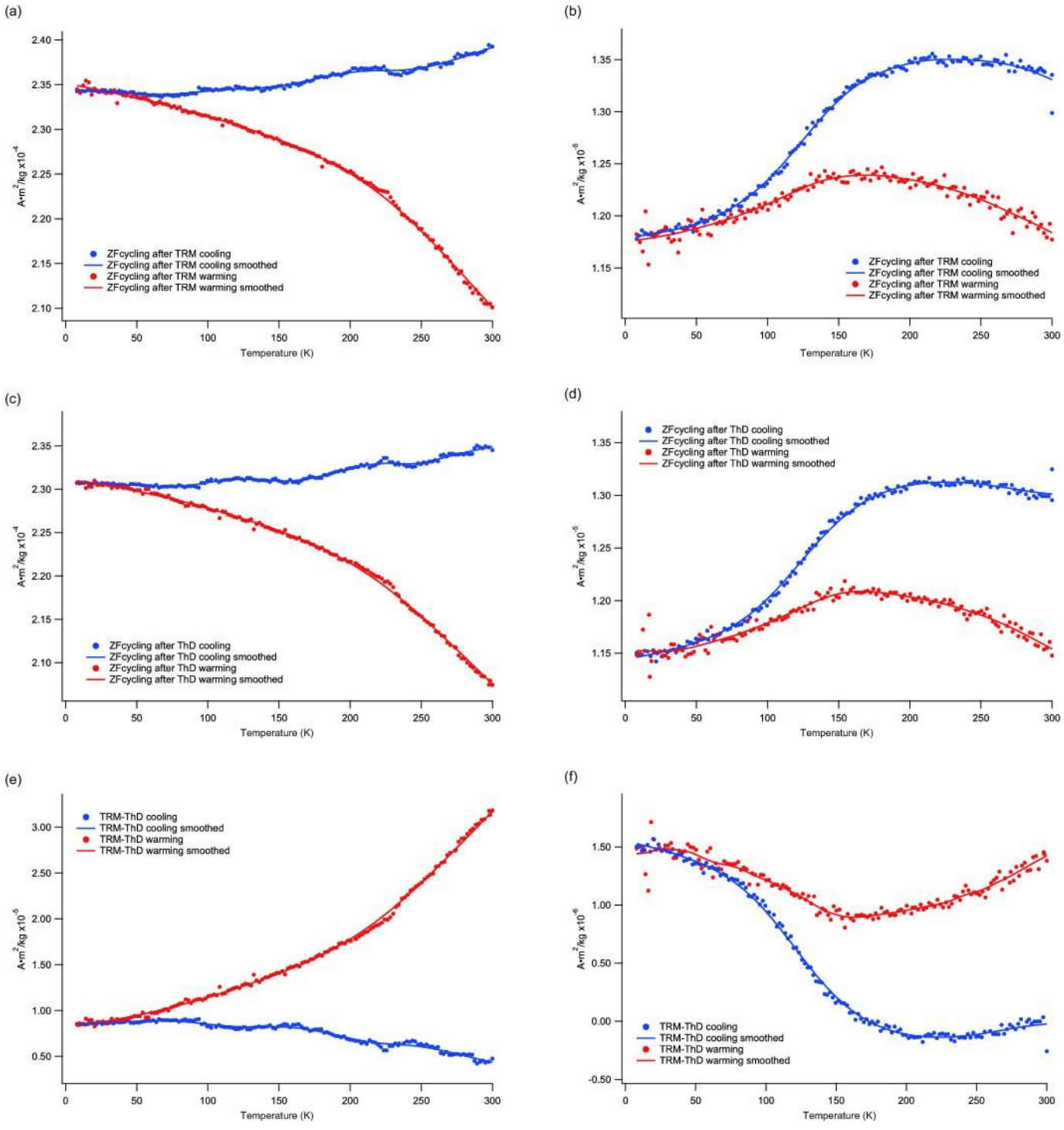


**Figure 5**

ZF-cycling curves after TRM at 400 K of (a) AAC-B2 and (b) AAC-W2; ZF-cycling curves after ThD at 400 K of (c) AAC-B3 and (d) AAC-W3; the difference between ZF-cycling curves after TRM and ZF-cycling curves after ThD of (e) AAC-B3 and (f) AAC-W3.

# Supplementary Files

This is a list of supplementary files associated with this preprint. Click to download.

- graphicalabstract.jpg
- Supplementaryfigure4.pdf
- SupplementaryFigure3.pdf
- SupplementaryFigure1.png
- SupplementaryFigure2.pdf